#### **OPEN ACCESS**



# New Evidence for Wet Accretion of Inner Solar System Planetesimals from Meteorites Chelyabinsk and Benenitra

Ziliang Jin<sup>1,2</sup>, Maitrayee Bose<sup>1</sup>, Tim Lichtenberg<sup>3</sup>, and Gijs D. Mulders<sup>4,5</sup>, school of Earth and Space Exploration, Arizona State University, Tempe, AZ 85287, USA; zljin@must.edu.mo

State Key Laboratory of Lunar and Planetary Sciences, Macau University of Science and Technology, Taipa, Macau, People's Republic of China Atmospheric, Oceanic and Planetary Physics, Department of Physics, University of Oxford, UK

Facultad de Ingeniería y Ciencias, Universidad Adolfo Ibáñez, Peñalolén, Santiago, Chile

Millennium Institute for Astrophysics, Chile

Received 2021 January 25; revised 2021 November 12; accepted 2021 November 24; published 2021 December 23

#### **Abstract**

We investigated the hydrogen isotopic compositions and water contents of pyroxenes in two recent ordinary chondrite falls, namely, Chelyabinsk (2013 fall) and Benenitra (2018 fall), and compared them to three ordinary chondrite Antarctic finds, namely, Graves Nunataks GRA 06179, Larkman Nunatak LAR 12241, and Dominion Range DOM 10035. The pyroxene minerals in Benenitra and Chelyabinsk are hydrated ( $\sim$ 0.018–0.087 wt.% H<sub>2</sub>O) and show D-poor isotopic signatures ( $\delta D_{SMOW}$  from -444% to -49%). On the contrary, the ordinary chondrite finds exhibit evidence of terrestrial contamination with elevated water contents ( $\sim$ 0.039–0.174 wt.%) and  $\delta D_{SMOW}$  values (from -199% to -14%). We evaluated several small parent-body processes that are likely to alter the measured compositions in Benenitra and Chelyabinsk and inferred that water loss in S-type planetesimals is minimal during thermal metamorphism. Benenitra and Chelyabinsk hydrogen compositions reflect a mixed component of D-poor nebular hydrogen and water from the D-rich mesostases. A total of 45%–95% of water in the minerals characterized by low  $\delta D_{SMOW}$  values was contributed by nebular hydrogen. S-type asteroids dominantly composed of nominally anhydrous minerals can hold 254–518 ppm of water. Addition of a nebular water component to nominally dry inner solar system bodies during accretion suggests a reduced need of volatile delivery to the terrestrial planets during late accretion.

Unified Astronomy Thesaurus concepts: Planet formation (1241); Chondrites (228); Meteorites (1038)

## 1. Introduction

In the inner solar system, water is present in the terrestrial planets, as evident from the vast amounts of water that cover Earth's surface and are contained in its deep interior (e.g., Peslier et al. 2017), the subglacial liquid water detected in the polar region of Mars (e.g., Orosei et al. 2018), the surface water ice in permanently shadowed regions of Mercury (e.g., Lawrence et al. 2013), and the water vapor measured in Venus's atmosphere (e.g., Cottini et al. 2012). However, in the standard picture of planetary accretion, the location of the water snowline outside of the terrestrial planet formation region necessitates the addition of water-rich materials from fartherout regions (Raymond & Izidoro 2017). Thus, the processes and timing of acquisition of water by the terrestrial planets are a long-standing question in planetary science, and no consensus has been reached yet.

Several scenarios have been proposed to explain the source and delivery of water to the inner solar system based on the studies of hydrogen isotopic composition of planetary materials. The most popular scenario argues that water was delivered to Earth by the water-rich objects from the outer solar system, e.g., C-type asteroids or comets, during different periods of planetary formation (e.g., Alexander et al. 2012; Sarafian et al. 2014). This scenario is based on the assumption that the building blocks of terrestrial planets were dry. However, D/H ratios of comets measured remotely do not

Original content from this work may be used under the terms of the Creative Commons Attribution 4.0 licence. Any further distribution of this work must maintain attribution to the author(s) and the title of the work, journal citation and DOI.

well match that of Earth's water, although one of the Jupiterfamily comets 103P/Hartley 2 has comparable water to Earth (e.g., Hutsemekers et al. 2008; Altwegg et al. 2015; Hartogh et al. 2011). In addition, although D/H ratios of CM and CI chondrites are comparable to those of terrestrial rocks, it is unlikely that C-type materials delivered a significant fraction of water to Earth. This is because, in addition to water, C-type asteroids would have brought significant amounts of siderophile elements, e.g., Os and Ru, and these elements show distinct isotopic compositions from terrestrial materials (Meisel et al. 1996; Fischer-Gödde & Kleine 2017). It has been suggested that Earth should have incorporated more than 70% of its hydrogen prior to the late chondritic veneer (Halliday 2013). Similarly, bulk abundance ratios of atmorbile elements in Earth (Hirschmann 2016) and Venus's present-day atmosphere (Gillmann et al. 2020) provide evidence against an overly volatile-rich composition of late-accreted material to the terrestrial planet region. Instead, this supports the addition of an early, indigeneous source of water to the inner solar system planets.

Ingassing of nebular hydrogen into the magma ocean on a differentiating rocky planet has been invoked to explain the addition of hydrogen into Earth's interior because the solar nebular gas characterized by a low D/H ratio  $(2.1 \times 10^{-5};$  Geiss & Gloeckler 1998) was likely present during Earth's initial growth stages (Ikoma & Genda 2006; Sharp 2017). However, the solubility of hydrogen molecules in silicate melts is dependent on the atmosphere pressure above the surface of the magma ocean (Hirschmann et al. 2012), which is not well constrained, and hence brings huge uncertainties on the amount of dissolved hydrogen. For instance, under a redox condition

corresponding to the iron-wüstite buffer, solubility of H in the magma ocean rises from 10 to 40 ppm (equivalent to 90–360 ppm water) as the atmosphere pressure increases from 0.1 to 1 bar (Hirschmann et al. 2012). Furthermore, the accretion of gaseous hydrogen envelopes tested through 1D gas accretion models (Coleman et al. 2019) shows that Earthsize planets could only accrete about 1% of their total mass in gas during its growth period, and the ingassing process became particularly slow during the post-solid-accretion phase. The possibility of the accreted envelope to be stripped away via irradiation by the central star is high, especially closer to the star (Lammer et al. 2018; Owen 2019). More importantly, the ingassing scenario is not an efficient process for small planetesimals (<250 km). The recently measured hydrogen isotopic compositions of the planetesimal population, including Itokawa regolith minerals and enstatite chondrites, indicate that undifferentiated inner solar system small bodies contain a significant amount of D-depleted water (Jin & Bose 2019; Piani et al. 2020). Therefore, rather than the dissolved hydrogen in the magma ocean, the undifferentiated small bodies containing hydrogen (in various forms) are a more likely source of water for terrestrial planets.

In order to determine the source of water in the inner solar system bodies and evaluate the processes by which terrestrial planets can acquire water through planetary accretion, we investigated the D/H ratios and water contents of silicate minerals from two recent ordinary chondrite (OC) falls and three Antarctic OC finds. In light of these analytical results, we evaluated the parent-body processes that might have modified the measured hydrogen signatures. We report high water contents and variable D/H ratios of the measured minerals; several grains in Chelyabinsk and Benenitra OC falls are characterized by D-poor signatures, indicating the wet accretion of chondritic planetesimals in the inner solar system. As a consequence, the high water content of planetary embryos and planets formed through planetary accretion is well justified.

## 2. Samples and Analytical Methods

## 2.1. Sample Description and Preparation

Two OC falls are LL5 Chelyabinsk and L6 Benenitra. Chelyabinsk fell in Chelyabinskaya district, Russia, in 2013 February. The fragments were collected immediately after its fall. Benenitra was collected in the town of Benenitra, Madagascar, right after its fall on 2018 July 27. Three OC finds, namely, LL4 Graves Nunataks 06179 (GRA 06179), LL5 Larkman Nunatak 12241 (LAR 12241), and L6 Dominion Range 10035 (DOM 10035), are Antarctic meteorites, and their weathering scales are categorized as A/B, A, and B, respectively.

Fresh fragments of the OC falls were acquired from the Field Museum, Chicago. These samples were polished with no hydrogen-bearing lubricants ("dry polish"), mounted in 1-inch indium metal, and placed in the oven at 45°C for 1 week, before placing them in the ultra—high-vacuum chambers in the NanoSIMS 50L at Arizona State University (ASU). Because we wanted to measure hydrogen in the polished samples, addition of water or water-based organic solvents was completely avoided during the "dry polish." The polishing materials included diamond films with grain sizes of 6, 3, 1, and 0.5  $\mu$ m. Three OC finds were prepared as thin sections by Johnson Space Center.

## 2.2. Standard Description and Preparation

The standards used to calibrate the water contents during NanoSIMS measurements were ALV-519 (basaltic glass,  $1700\pm43$  ppm  $\rm\,H_2O$ ,  $1\sigma$ ; Saal et al. 2013, sessions 1–3), PMR-53 (clinopyroxene,  $268\pm8$  ppm  $\rm\,H_2O$ ,  $1\sigma$ ; Rossman et al. 1995, sessions 2–3), KH03–27 (orthopyroxene,  $367\pm49$  ppm  $\rm\,H_2O$ ,  $1\sigma$ ; Kumamoto et al. 2017, session 1), and 116610-18 (orthopyroxene,  $119\pm11$  ppm  $\rm\,H_2O$ ,  $1\sigma$ ; Kumamoto et al. 2017, used in sessions 1–3). ALV-519 ( $\delta \rm\,D_{SMOW} = -72\% c$ ; Saal et al. 2013) and PMR-53 ( $\delta \rm\,D_{SMOW} = -115\% c$ ; Bell & Ihinger 2000) were used to calibrate the D/H ratios of the minerals. The San Carlos olivine was used as the blank to monitor the background during NanoSIMS analyses.

The standards used during the IMS 6f session were ALV-519, 116610-18, and PMR-53. San Carlos olivine was used as the blank to calculate the hydrogen background.

Small chips of the acquired standards were first mounted in epoxy (EpoThin 2 Resin by Buehler) and dry-polished flat and smooth using sandpaper and diamond films. Then, we used pure acetone to partially dissolve the epoxy stub and pick out the polished standards. Subsequently, the polished standards were dried in the oven for several weeks, followed by mounting into 10 mm aluminum rings filled with indium (99.9% pure). In each NanoSIMS session, the meteorite and standard mounts were placed in the same holder so that they can be measured under identical conditions.

#### 2.3. Backscattered Electron Images and Elemental Mapping

Backscattered electron images (Figure 1) and X-ray intensity maps (Si, Ti, Al, Fe, Mg, Ca, Na, and K) of the meteorites were obtained using a JEOL JXA-8530F electron microprobe at ASU with an accelerating voltage of 15 keV, a beam current of 60 nA, a beam diameter of 20  $\mu$ m, and a dwell time of 30  $\mu$ s pixel<sup>-1</sup>. The elemental maps were used to estimate the volume fractions of mineral phases in the analyzed meteorites and to identify and select orthopyroxene minerals that were later measured for water contents and D/H ratios by the ion microprobes. The parent bodies of these type 5 and 6 meteorites are supposed to have experienced thermal metamorphism characterized by peak temperatures up to 1100 K (Gail & Trieloff 2019). The original chondritic silicate minerals, namely, olivine and pyroxene, crystallized from the precursor melts at temperatures of 1400 K would have survived under the high temperatures, whereas the chondrule metastasis and fine-grained matrix components recrystallized and formed new mineral phases, e.g., feldspar. We selected pyroxene grains (20–100  $\mu$ m) to measure because they are more resistant to thermal metamorphism than olivines in chondrules (Huss et al. 2006).

# 2.4. Secondary Ion Mass Spectrometry (SIMS)

Cameca NanoSIMS 50L. D/H ratios and  $\rm H_2O$  concentrations of the standards and orthopyroxenes from Chelyabinsk, Benenitra, GRA 06179, and DOM 10035 were measured by the Cameca NanoSIMS 50L. The NanoSIMS measurements were done in three sessions: (1) GRA 06179 and DOM 10035, (2) Benenitra, and (3) Chelyabinsk. A 220 pA Cs<sup>+</sup> primary beam with an approximate beam size of  $<2~\mu m$  (D1–3 aperture with diameter of 200  $\mu m$ ) was rastered on a  $15 \times 15~\mu m^2$  surface on the grains. Electronic gating was used to collect the secondary ion signal from the internal 25% of the rastered area.

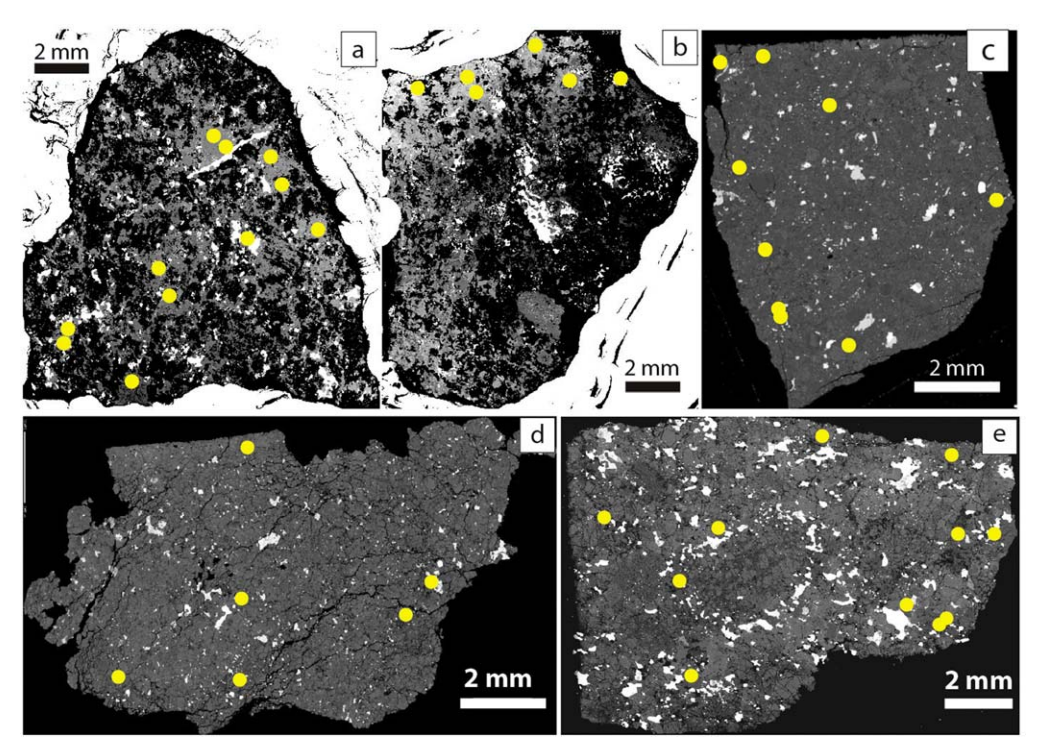


Figure 1. Backscattered electron images of OCs. The measured OCs are (a) Benenitra, (b) Chelyabinsk, (c) LL4 GRA 06179, (d) LL5 LAR 12241, and (e) L6 DOM 10035. The yellow circles show the analyzed spots with the SIMS instruments.

The primary beam has an impact energy of 16 keV. Prior to the data collection, the sample surface was presputtered for  $\sim\!10$  minutes in order to remove the surface contamination.  $^1H^-, ^2D^-, ^{12}C^-,$  and  $^{18}O^-$  were detected simultaneously with a 50  $\mu m$  entrance slit (ES1) and no aperture slit. The mass resolving power for the spectrometer was  $\sim\!1250$  (Cameca mass resolving power). Each measurement contained 200 cycles. During the analyses, the counting time for each pixel was  $300~\mu s$  pixel $^{-1}$ . To compensate for the charging of the sample surface, the electron gun ( $\sim\!80~\rm nA$ ) was employed. The pressure of the analysis chamber was better than  $2\times10^{-10}$  torr.

Cameca IMS 6f. The measurements of water contents and D/H ratios in the pyroxenes from LAR 12241 (Session 4) were performed on the Cameca IMS 6f at ASU. A 10–13 nA Cs<sup>+</sup> ion beam accelerated with an energy of 15 keV was rastered on a  $35 \times 35 \, \mu \text{m}^2$  surface area. The size of the primary beam was  $\sim 25 \, \mu \text{m}$ . The area of interest was presputtered for 2 minutes prior to analysis. The field aperture was set to 15  $\mu \text{m}$  diameter in order to reduce the crater edge effects. For each spot, 50 cycles measuring H<sup>-</sup> and D<sup>-</sup> were collected by an electron multiplier with counting times of 1 and 10 s, respectively. At the end of each measurement,  $^{16}\text{O}^-$  was measured using a Faraday cup. The mass resolving power during operation was  $\sim 800$ . The electron gun with a current of  $\sim 1 \, \mu \text{A}$  was used to compensate for surface charge during the measurements. The vacuum in the analytical chamber was  $\sim 3 \times 10^{-9}$  torr during analyses.

#### 2.5. Wavelength-dispersive X-Ray Spectroscopy (WDS)

The orthopyroxenes that have been analyzed using SIMS instruments were then measured using wavelength-dispersive X-ray spectroscopy. Prior to the WDS analysis, we checked the craters left by the SIMS measurements and only selected the areas with clean and flat craters to conduct the WDS measurements (Figure 2). The analyzed area on each mineral

grain was close to the SIMS crater. Analytical conditions were 15 keV acceleration voltage, 15 nA beam current, 1  $\mu$ m beam diameter, and counting times on the peaks and backgrounds of 40 s for Na and K and 60 s for Si, Ti, Al, Cr, Ca, Mg, Mn, and Fe. Well-characterized, natural and synthetic standards (K-hornblende, Ca-wollastonite, Al, Na-augite, Si, Mg-enstatite, Ti-rutile, Cr-chromite, Fe-fayalite) were used for calibration and to confirm the analytical precision. Detection limits were 0.02 wt.% for K<sub>2</sub>O, CaO, Al<sub>2</sub>O<sub>3</sub>, SiO<sub>2</sub>, Na<sub>2</sub>O, and MgO, 0.03 wt.% for TiO<sub>2</sub> and Cr<sub>2</sub>O<sub>3</sub>, and 0.06 wt.% for MnO and FeO; the relative error of the analyses was better than 0.3% for Si and Mg;  $\sim$ 1% for FeO;  $\sim$ 10% for Ca, Mn, and Cr; and larger than 20% for K, Al, Na, and Ti.

## 3. Results

#### 3.1. Petrologic Characterization

We estimated the mineral proportions of two meteorite falls, namely, Chelyabinsk and Benenitra, based on the X-ray elemental maps. The dominant silicate minerals in Chelyabinsk are olivine ( $60\pm 5$  vol.%) and low-Ca pyroxene ( $30\pm 5$  vol.%), consistent with previous reports (Ozawa et al. 2014; Kaeter et al. 2018). A smaller fraction of feldspars (<10 vol.%) and Fe-Ni metal (<5 vol.%) also occurs in the interstitial areas (Figures 2(a) and (b)). The fragment of Benenitra consists of olivine ( $55\pm 5$  vol.%) and pyroxene ( $30\pm 5$  vol.%), interstitial feldspars (<10 vol.%), and Fe-Ni metals (Figures 2(c) and (d)). The original matrix and chondrule mesostasis components in the two meteorites are absent because they have experienced extensive thermal metamorphism.

## 3.2. Water Contents

In nominally anhydrous minerals (NAMs), hydrogen generally occurs in the defects of the crystal, because a normal

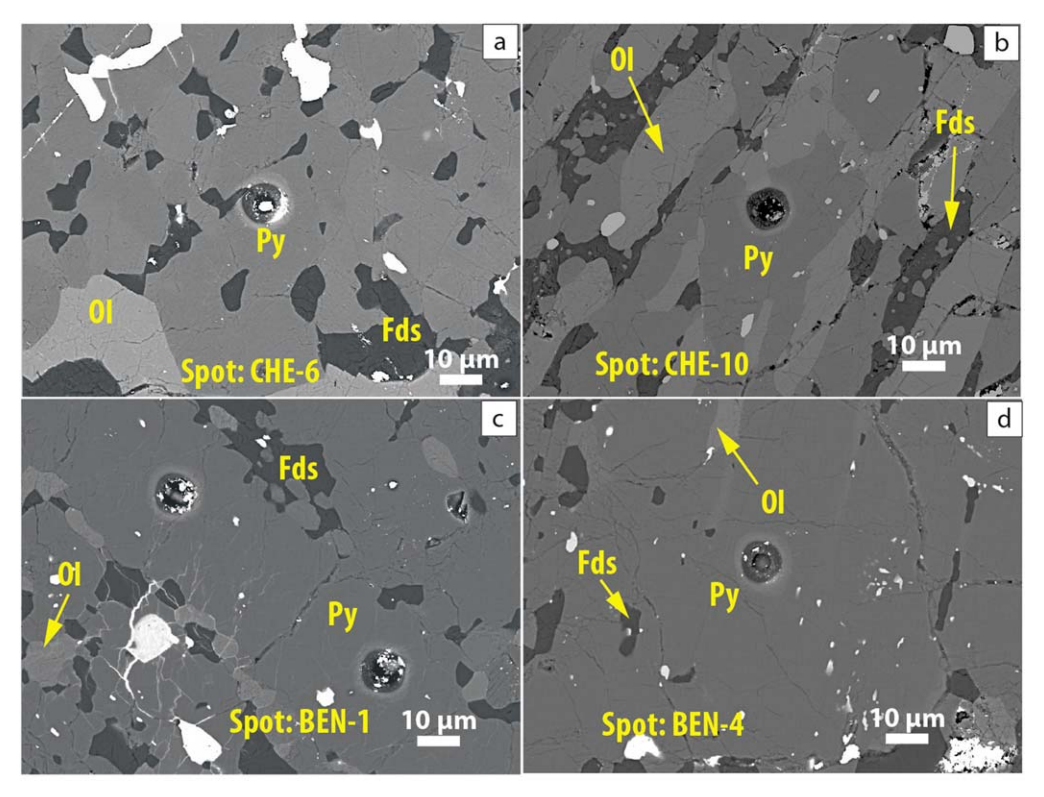


Figure 2. Representative backscattered electron images of Chelyabinsk (panels (a)–(b)) and Benenitra (panels (c)–(d)). The major silicate minerals in both OCs are olivine (Ol) and pyroxene (Py). Feldspars (Fds) occur in the interstitial areas. The small craters were generated after NanoSIMS measurements.

lattice site cannot be occupied by hydrogen. For instance, the vacancies of Mg and Si in NAMs can be occupied by hydrogen via substitutions  $2H^+ \rightarrow Mg^{2+}$  and  $H^+ + Al^{3+} \rightarrow Si^{4+}$  (Bell & Rossman 1992; Hauri et al. 2006). These hydrogen ions preferentially combine with the adjacent oxygen ions and form structurally bound O-H in the crystal lattice. The O-H bonds in the crystal act as the proxy for water. During SIMS measurements, the O-H bonds are broken by the primary ion beam. The released secondary H<sup>+</sup> ions were subsequently collected by the detector on the instrument. Accordingly, we estimated the water contents of the measured pyroxenes in both OC falls and finds by using the H<sup>-</sup>/O<sup>-</sup> versus H<sub>2</sub>O calibration line. We first plotted the measured  $H^-/O^-$  ratios of the standards versus their reported water contents in previous literature (Figure 3). Then, we used the slopes and the intercept values of the calibration lines and the H<sup>-</sup>/O<sup>-</sup> ratios of the measured pyroxenes in OC samples to calculate their water contents. The low H<sup>-</sup>/O<sup>-</sup> values of San Carlos olivine correspond to background water of 65, 34, 67, and <15 ppm for sessions 1-4. The uncertainties on the water contents in the samples were obtained by propagating the uncertainties on the H<sup>-</sup>/O<sup>-</sup> ratios and slopes of the calibration trendlines.

The water contents of orthopyroxenes from OC finds and falls are listed in Table 1. The minerals from OC finds have water contents of 458–1807 ppm weight. In OC falls, the measured orthopyroxenes have water contents of 210–902 ppm. After subtracting the water from the background, the water contents of pyroxenes in OC finds are 393–1742 ppm (median =  $844 \pm 173$  ppm) and in OC falls contain 176–868 ppm water (median =  $558 \pm 116$  ppm). The water contents of pyroxene minerals in OC falls (176–868 ppm) are comparable to those of the returned Itokawa pyroxene minerals (278–988 ppm; Jin & Bose 2019; Chan et al. 2021), yet the upper limit (868 ppm) is lower than that

observed in several pyroxenes from the Type 3 OC Bishunpur (1796 ppm; Stephant et al. 2017). In contrast, our results are all higher than the reported water content of one pyroxene grain from the Type 3.05 OC QUE 97008 (12 ppm; Shimizu et al. 2021).

#### 3.3. Hydrogen Isotopes

During SIMS measurements, the instrumental mass fractionation (IMF) as a result of the sputtering process, transmission efficiency, and ion detection efficiency can cause systematic bias in the data, which must be corrected. The IMF is defined as

$$IMF = \frac{(D/H)_{MEAS} - (D/H)_{TRUE}}{(D/H)_{TRUE}},$$
(1)

where  $(D/H)_{MEAS}$  is the measured ratio and  $(D/H)_{TRUE}$  is the real isotopic ratio of the sample. The real and measured D/H ratios of ALV-519  $((D/H)_{TRUE} = 1.4454 \times 10^{-4})$  and PMR-53  $((D/H)_{TRUE} = 1.3784 \times 10^{-4})$  were used to calculate the IMFs during the analyses. In session 1, the average IMF of ALV-519 is  $0.490 \pm 0.053$  (N = 6,  $1\sigma$ ). In sessions 2 and 3, the IMFs of ALV-519 and PMR-53 are similar within errors in each session. We then employed the average IMF of the utilized references (ALV-519 and PMR-53), which are  $-0.041 \pm 0.039$  (N = 8,  $1\sigma$ ) for session 2 and  $-0.078 \pm 0.021$  (N = 6,  $1\sigma$ ) for session 3. The IMF for IMS 6f measurements is  $-0.013 \pm 0.019$  (Session 4, N = 4,  $1\sigma$ ).

Using these IMF numbers, we obtained the true D/H ratios of measured minerals. Then, we made the background correction for the D/H ratios ((D/H)<sub>CORR</sub>) by subtracting the portion of D and H contributed by the background hydrogen. These corrected D/H ratios were normalized to standard mean

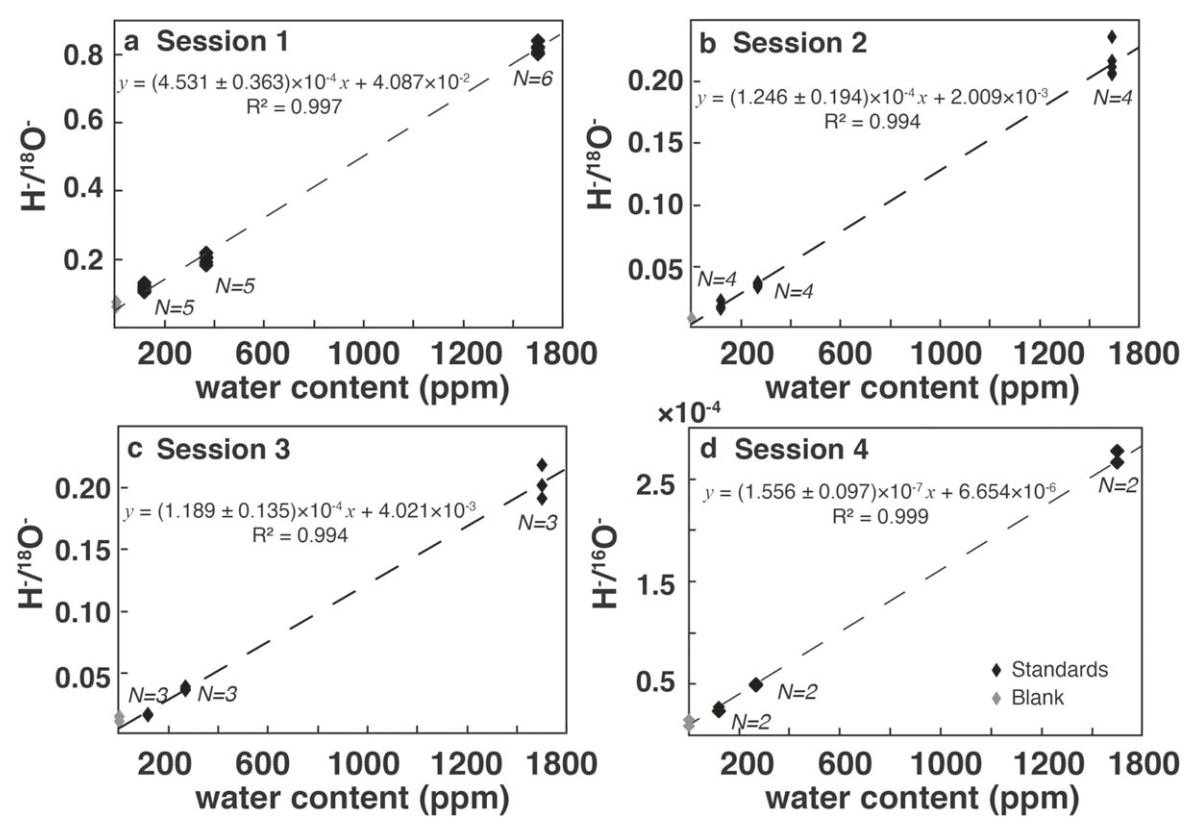


Figure 3. Calibrations of water contents and hydrogen isotope compositions using terrestrial mineral and glass standards. The measured H/O ion ratios vs.  $H_2O$  contents derived through bulk measurements are plotted. The trendlines shown in the diagrams were used to estimate the water contents of the measured pyroxenes in sessions 1–4 (panels (a)–(d)). The standards are ALV-519 (basaltic glass,  $1700 \pm 43$  ppm  $H_2O$ ), PMR-53 (clinopyroxene,  $268 \pm 8$  ppm  $H_2O$ ), KH03–27 (orthopyroxene,  $367 \pm 49$  ppm  $H_2O$ ), and 116610-18 (orthopyroxene,  $119 \pm 11$  ppm  $H_2O$ ). Blank monitor: San Carlos olivine.

ocean water (SMOW, D/H =  $1.5576 \times 10^{-4}$ ) via

$$\delta D_{\text{SMOW}}(\%) = \left(\frac{(D/H)_{\text{CORR}}}{(D/H)_{\text{SMOW}}} - 1\right) * 1000.$$
 (2)

The D/H ratios and associated errors of orthopyroxenes from OC finds and falls are listed in Table 1. Uncertainties on the D/H ratios and the IMF were propagated to calculate the uncertainties on the  $\delta D_{SMOW}$  values. The  $\delta D_{SMOW}$  values are plotted against the measured water contents in Figure 3. The  $\delta D_{SMOW}$  values of measured minerals from OC finds vary from -199% to -14% (median = -129%  $\pm 24\%$ ). The measured pyroxenes from OC falls have more negative  $\delta D_{SMOW}$  values varying from -444% to -49%, with a median value of -263%  $\pm 63\%$ .

#### 3.4. Major Element Abundances

The measured minerals from the OC finds have similar major element compositions. They have MgO contents of 24.30-30.43 wt.% and FeO contents of 12.30-18.02 wt.%. The  $Al_2O_3$  contents of measured minerals in OC finds mostly fall in a range of 0.10-0.32 wt.%, except for one grain that has 2.24 wt.%  $Al_2O_3$  (Table 2). The composition range of the three end members (Wollastonite (Wo)-Enstatite (En)-Ferrosilite (Fs)) is  $Wo_{0.4-3.9}En_{70.4-81.0}Fs_{18.4-27.6}$ . The measured minerals from these OC falls have MgO contents of 27.36-29.40 wt.%, FeO contents of 13.58-15.91 wt.%, and  $Al_2O_3$  contents of 0.08-0.21 wt.% (Table 2). Their Wo-En-Fs compositions are

similar to those of OC finds and have a range of  $Wo_{0.9-2.0}En_{74.5-78.1}Fs_{20.5-24.1}$ .

## 4. Discussion

## 4.1. A Source of Low D/H Ratios in Benenitra and Chelyabinsk

As shown in Figure 4, the  $\delta D_{SMOW}$  values of orthopyroxene minerals in OC finds are distinguishable from those in OC falls, although there is some overlap. For clarity, we made the boxand-whisker plots (Figure 5), in which minerals in OC finds exhibit elevated interquartile ranges of both  $\delta D_{SMOW}$  values and water contents relative to those of OC falls. Previous studies have revealed that Antarctic meteorites subjected to terrestrial weathering can cause localized mobilization of both major elements (e.g., Si and Mg; Velbel 2014) and trace elements (e.g., rare earth elements; Crozaz et al. 2003). In addition, terrestrial exposure experiment conducted on the Martian meteorite fall Tissint showed that terrestrial weathering can rapidly affect the hydrogen isotopic ratios and water contents of olivines (Stephant et al. 2018). Therefore, long-term exposure in Antarctic ice has likely altered the original hydrogen signatures in small stones and caused the elevation of  $\delta D_{SMOW}$  values and water contents in chondritic minerals. Furthermore, the Antarctic thin sections use tiny amounts of epoxy resin, which may be the likely reason for the elevated water contents and terrestrial-like D/H ratios in the OC falls (Mane et al. 2016). The contamination signal from the resin introduced during thin section preparation of the OC finds in this study cannot be completely avoided during SIMS measurements. Thus, Antarctic meteorite finds are not

Table 1

Hydrogen Isotopic Compositions and Water Contents of Pyroxene Minerals in Ordinary Chondrite Falls and Finds

Sample	D/H <sup>a</sup>	$1\sigma$	$\delta D_{SMOW}$	$1\sigma$	Water Content (ppm) <sup>a</sup>	$1\sigma$	
		Nano	SIMS Session 1				
GRA 06179-1	$1.46 \times 10^{-4}$	$7.85 \times 10^{-6}$	-63	34	773	67	
GRA 06179-2	$1.38 \times 10^{-4}$	$6.80 \times 10^{-6}$	-112	29	746	65	
GRA 06179-3	$1.42 \times 10^{-4}$	$6.99 \times 10^{-6}$	-89	30	712	62	
GRA 06179-5	$1.41 \times 10^{-4}$	$9.67 \times 10^{-6}$	-92	42	393	37	
GRA 06179-6	$1.49 \times 10^{-4}$	$7.74 \times 10^{-6}$	-42	33	670	59	
GRA 06179-7	$1.28 \times 10^{-4}$	$6.75 \times 10^{-6}$	-180	29	954	82	
GRA 06179-8	$1.35 \times 10^{-4}$	$6.85 \times 10^{-6}$	-136	29	1139	97	
GRA 06179-10	$1.38 \times 10^{-4}$	$5.62 \times 10^{-6}$	-113	24	1250	105	
GRA 06179-11	$1.33 \times 10^{-4}$	$6.74 \times 10^{-6}$	-145	29	862	74	
GRA 06179-12	$1.34 \times 10^{-4}$	$8.82 \times 10^{-6}$	-142	38	475	43	
DOM 10035-1	$1.28 \times 10^{-4}$	$8.96 \times 10^{-6}$	-180	38	1118	95	
DOM 10035-2	$1.47 \times 10^{-4}$	$8.04 \times 10^{-6}$	-57	35	1070	91	
DOM 10035-3	$1.34 \times 10^{-4}$	$8.18 \times 10^{-6}$	-141	35	844	73	
DOM 10035-4	$1.26 \times 10^{-4}$	$9.08 \times 10^{-6}$	-192	39	632	56	
DOM 10035-5	$1.37 \times 10^{-4}$	$8.91 \times 10^{-6}$	-119	38	719	63	
DOM 10035-7	$1.34 \times 10^{-4}$	$6.90 \times 10^{-6}$	-140	30	1718	143	
DOM 10035 7	$1.32 \times 10^{-4}$	$6.78 \times 10^{-6}$	-156	29	1742	145	
DOM 10035-11 DOM 10035-12	$1.25 \times 10^{-4}$	$1.08 \times 10^{-5}$	-199	47	479	44	
DOM 10035-12 DOM 10035-13	$1.28 \times 10^{-4}$	$1.22 \times 10^{-5}$	-179 -179	53	477	43	
DOM 10035-13 DOM 10035-14	$1.28 \times 10^{-4}$ $1.46 \times 10^{-4}$	$8.64 \times 10^{-6}$	-179 -64	37	1092	93	
DOM 10035-14 DOM 10035-15	$1.36 \times 10^{-4}$	$7.27 \times 10^{-6}$	-129	31	1208	102	
		Nanc	SIMS Session 2				
Ben-1	$1.23 \times 10^{-4}$	$2.52 \times 10^{-6}$	-210	36	653	106	
Ben-3	$8.66 \times 10^{-5}$	$5.84 \times 10^{-6}$	-444	46	305	53	
Ben-4	$1.04 \times 10^{-4}$	$4.93 \times 10^{-6}$	-331	44	176	33	
Ben-5	$1.36 \times 10^{-4}$	$3.94 \times 10^{-6}$	-130	44	342	58	
Ben-6	$1.01 \times 10^{-4}$	$3.86 \times 10^{-6}$	-349	37	465	77	
Ben-7	$1.01 \times 10^{-4}$ $1.15 \times 10^{-4}$	$2.94 \times 10^{-6}$	-263	36	868	140	
Ben-8	$1.04 \times 10^{-4}$	$2.96 \times 10^{-6}$	-333	34	446	74	
Ben-9	$1.04 \times 10$ $1.23 \times 10^{-4}$	$2.65 \times 10^{-6}$	-333 -214	36	679	110	
	$1.25 \times 10^{-4}$ $1.25 \times 10^{-4}$	$3.16 \times 10^{-6}$	-214 $-201$	39	558	92	
Ben-10	$1.23 \times 10$ $1.07 \times 10^{-4}$	$2.34 \times 10^{-6}$	-201 -311	32			
Ben-12	$1.07 \times 10$ $1.00 \times 10^{-4}$	$2.34 \times 10^{-6}$ $2.27 \times 10^{-6}$			720 657	117	
Ben-13	1.00 × 10		-356	31	037	107	
			SIMS Session 3				
Che-5	$9.37 \times 10^{-5}$	$2.22 \times 10^{-6}$	-398	21	524	67	
Che-6	$1.18 \times 10^{-4}$	$2.35 \times 10^{-6}$	-244	16	690	86	
Che-7	$1.36 \times 10^{-4}$	$2.76 \times 10^{-6}$	-124	19	432	57	
Che-8	$1.48 \times 10^{-4}$	$3.37 \times 10^{-6}$	-49	23	382	51	
Che-9	$1.23 \times 10^{-4}$	$2.04 \times 10^{-6}$	-210	14	749	93	
Che-10	$1.13 \times 10^{-4}$	$1.97 \times 10^{-6}$	-277	14	773	95	
			S 6f Session 4				
LAR12141-2	$1.30 \times 10^{-4}$	$1.14 \times 10^{-6}$	-167	50	794	51	
LAR12141-5	$1.40 \times 10^{-4}$	$1.83 \times 10^{-6}$	-104	55	489	31	
LAR12141-6	$1.54 \times 10^{-4}$	$1.35 \times 10^{-6}$	-14	59	717	46	
LAR12141-8	$1.43 \times 10^{-4}$	$1.41 \times 10^{-6}$	-81	56	992	63	
LAR12141-10	$1.27 \times 10^{-4}$	$2.16 \times 10^{-6}$	-187	51	871	55	
LAR12141-11	$1.41 \times 10^{-4}$	$1.96 \times 10^{-6}$	-94	56	1468	93	

#### Note.

necessarily the best samples for hydrogen (and other volatile) analyses. Inferences about small Antarctic stones, especially thin sections prepared in epoxy, should be made with caution.

Chelyabinsk and Benenitra were immediately collected and well preserved after they fell on Earth. Besides, the careful handling of the samples during polishing and mounting and the analysis of thick rock sections with no epoxy would keep terrestrial contamination to a minimum. Several parent-body processes could have modified the original compositions of hydrogen in the minerals. These processes include (i) electron irradiation (e.g., Laurent et al. 2015), (ii) galactic cosmic-ray (GCR) spallation (e.g., Füri et al. 2017), and (iii) heating events (e.g., Huss et al. 2006). Below we discuss each of these processes and their effects on the hydrogen component.

<sup>&</sup>lt;sup>a</sup> Background corrected.

Table 2
Chemical Compositions of the Measured Pyroxenes in the OC Meteorites

<b>G</b>	SiO <sub>2</sub>	TiO <sub>2</sub>	$Al_2O_3$	FeO	MnO	MgO	CaO	Na <sub>2</sub> O	K <sub>2</sub> O	$Cr_2O_3$	Total	W (61)	F (0()	F (6()
Spot	(wt.%)	(wt.%)	(wt.%)	(wt.%)	(wt.%)	(wt.%)	(wt.%) Finds	(wt.%)	(wt.%)	(wt.%)	(wt.%)	Wo (%)	En (%)	Fs (%)
GRA 06179-1	55.13	0.04	0.26	14.94	0.47	28.54	0.31	bdl	0.00	0.26	99.94	0.6	76.8	22.6
GRA 06179-2	54.42	0.16	0.32	14.22	0.51	27.63	2.01	0.03	0.01	0.33	99.63	3.9	74.6	21.5
GRA 06179-3	55.29	0.01	0.13	14.21	0.48	29.23	0.29	0.02	0.00	0.19	99.86	0.6	78.1	21.3
GRA 06179-5	55.94	0.02	0.12	12.30	0.40	30.43	0.32	0.01	0.01	0.23	99.76	0.6	81.0	18.4
GRA 06179-6	54.00	0.11	2.24	15.50	0.41	24.30	1.87	0.11	0.05	0.36	98.95	3.9	70.8	25.3
GRA 06179-7	55.17	0.09	0.10	15.09	0.49	28.43	0.72	0.01	0.02	0.14	100.25	1.4	76.0	22.6
GRA 06179-8	55.60	0.02	0.14	13.74	0.37	29.69	0.20	0.00	0.01	0.18	99.93	0.4	79.1	20.5
GRA 06179-10	54.15	0.18	0.14	16.30	0.49	26.57	1.32	0.04	0.01	0.15	99.34	2.6	72.5	24.9
GRA 06179-11	54.19	0.18	0.11	16.07	0.53	26.73	1.32	0.02	0.00	0.12	99.27	2.6	72.8	24.6
GRA 06179-12	54.06	0.05	0.22	14.84	0.49	28.58	0.30	0.02	0.02	0.21	98.80	0.6	77.0	22.4
DOM 10035-1	55.39	0.12	0.12	13.66	0.48	28.99	0.94	0.02	0.03	0.15	99.90	1.8	77.7	20.5
DOM 10035-2	55.18	0.19	0.16	13.66	0.47	28.89	0.84	0.01	0.02	0.13	99.55	1.6	77.8	20.6
DOM 10035-3	54.95	0.15	0.15	13.85	0.50	28.49	0.77	0.04	0.02	0.10	99.01	1.5	77.4	21.1
DOM 10035-4	55.50	0.14	0.12	13.88	0.51	29.25	0.90	0.01	0.01	0.14	100.46	1.7	77.6	20.7
DOM 10035-5	55.46	0.19	0.17	13.99	0.51	28.71	1.12	0.02	0.00	0.15	100.34	2.2	76.8	21.0
DOM 10035-7	55.03	0.16	0.15	14.40	0.45	28.85	0.89	0.01	0.03	0.13	100.11	1.7	76.8	21.5
DOM 10035-11	55.49	0.18	0.18	13.94	0.49	29.02	0.85	0.01	0.02	0.10	100.27	1.6	77.5	20.9
DOM 10035-12	55.27	0.19	0.16	13.94	0.50	28.68	0.80	bdl	bdl	0.11	99.64	1.5	77.4	21.1
DOM 10035-13	55.32	0.18	0.16	13.40	0.54	28.77	1.07	0.03	0.01	0.15	99.62	2.1	77.6	20.3
DOM 10035-14	55.60	0.18	0.17	13.77	0.47	28.96	0.83	0.01	0.01	0.12	100.11	1.6	77.7	20.7
DOM 10035-15	55.52	0.20	0.18	13.81	0.45	28.76	1.00	0.02	0.00	0.19	100.13	1.9	77.3	20.8
LAR 12241-2	54.69	0.21	0.20	16.69	0.50	26.64	1.16	0.04	bdl	0.17	100.30	2.3	72.3	25.4
LAR 12241-5	55.02	0.19	0.16	16.47	0.47	27.02	0.99	0.00	bdl	0.16	100.45	1.9	73.1	25.0
LAR 12241-6	53.99	0.09	0.11	16.49	0.43	26.90	1.22	0.03	0.02	0.12	99.41	2.4	72.6	25.0
LAR 12241-8	53.47	0.17	0.18	18.02	0.43	25.74	0.99	0.03	0.02	0.11	99.16	1.9	70.4	27.6
LAR 12241-10	54.29	0.18	0.19	16.72	0.49	27.05	0.99	0.01	0.02	0.11	100.04	1.9	72.8	25.3
LAR 12241-11	54.59	0.21	0.16	16.76	0.49	26.97	1.15	0.02	0.02	0.14	100.52	2.2	72.5	25.3
						OC	Falls							
BEN-1	55.57	0.18	0.15	13.99	0.49	29.13	0.55	0.01	0.03	0.08	100.18	1.1	77.9	21.0
BEN-3	55.64	0.17	0.15	13.88	0.45	29.01	0.82	0.03	0.01	0.15	100.32	1.6	77.6	20.8
BEN-4	55.68	0.22	0.11	14.12	0.50	29.13	0.49	0.01	0.03	0.11	100.40	0.9	77.9	21.2
BEN-5	55.52	0.21	0.21	13.77	0.45	28.83	1.02	0.03	0.01	0.16	100.22	2.0	77.3	20.7
BEN-6	55.69	0.17	0.16	14.05	0.50	29.03	0.77	bdl	0.02	0.12	100.50	1.5	77.5	21.0
BEN-7	55.79	0.17	0.17	13.58	0.50	29.04	0.75	bdl	0.01	0.10	100.11	1.5	78.1	20.5
BEN-8	55.69	0.16	0.13	14.07	0.50	29.22	0.69	0.01	bdl	0.10	100.57	1.3	77.7	21.0
BEN-9	55.77	0.19	0.17	13.99	0.48	28.86	0.89	bdl	0.00	0.12	100.46	1.7	77.3	21.0
BEN-10	55.70	0.21	0.15	13.73	0.51	28.89	0.70	0.01	0.02	0.12	100.04	1.4	77.9	20.8
BEN-12	56.25	0.12	0.08	13.76	0.49	29.40	0.70	bdl	bdl	0.06	100.85	1.3	78.1	20.5
BEN-13	55.96	0.11	0.10	13.97	0.51	29.26	0.78	0.01	0.02	0.06	100.78	1.5	77.7	20.8

Table 2 (Continued)

Spot	SiO <sub>2</sub> (wt.%)	TiO <sub>2</sub> (wt.%)	Al <sub>2</sub> O <sub>3</sub> (wt.%)	FeO (wt.%)	MnO (wt.%)	MgO (wt.%)	CaO (wt.%)	Na <sub>2</sub> O (wt.%)	K <sub>2</sub> O (wt.%)	Cr <sub>2</sub> O <sub>3</sub> (wt.%)	Total (wt.%)	Wo (%)	En (%)	Fs (%)
CHE-5	54.78	0.17	0.15	15.56	0.42	27.85	0.77	bdl	0.02	0.12	99.82	1.5	75.0	23.5
CHE-6	54.77	0.18	0.14	15.57	0.48	27.76	0.86	0.05	0.00	0.09	99.89	1.7	74.8	23.5
CHE-7	54.86	0.15	0.16	15.91	0.43	27.58	0.70	0.02	bdl	0.07	99.88	1.4	74.5	24.1
CHE-8	54.90	0.14	0.11	15.49	0.46	27.84	0.84	0.00	0.04	0.09	99.90	1.6	75.0	23.4
CHE-9	54.43	0.19	0.13	15.66	0.39	27.36	0.68	0.01	0.02	0.11	98.97	1.3	74.7	24.0
CHE-10	54.96	0.16	0.11	15.57	0.41	27.58	0.64	bdl	0.01	0.16	99.59	1.3	75.0	23.7

#### Note.

<sup>&</sup>lt;sup>a</sup> bdl: below detection limit.

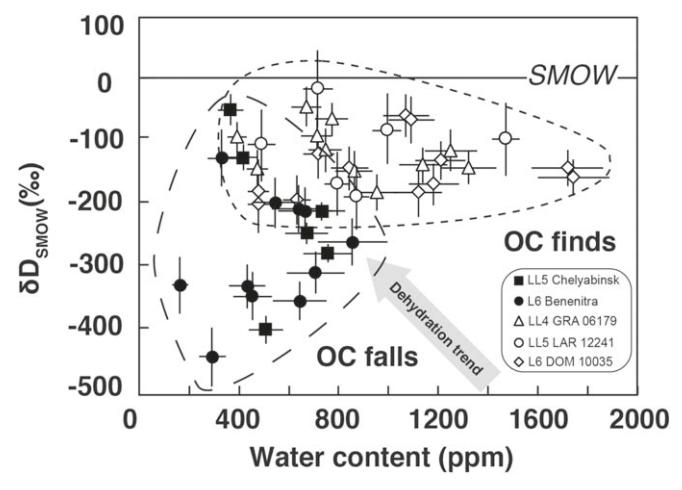


Figure 4. Water contents (ppm) and  $\delta D_{SMOW}$  values (‰) of pyroxenes from OC falls and finds. Minerals from OC falls have distinguishable and much lower  $\delta D_{SMOW}$  values (as low as -444%0 observed in Benenitra) and water contents than those of minerals from OC finds. No clear dehydration trend is observed. Errors are one standard deviation. SMOW: standard mean ocean water

(i) Electron irradiation. Electron irradiation can induce heating of the sample and ionization of hydrogen atoms from the surface of solids, resulting in hydrogen loss coupled with deuterium enrichment of the solid residue (Laurent et al. 2015). Thus, it is possible that D/H ratios in silicate minerals freely floating in the protosolar nebula prior to accretion or on the surface of the parent bodies are modified by electron irradiation. Previous experiments by Roskosz et al. (2016) reported that electrons in the keV regime have the capacity to produce large D-enrichment (fractionation of D/H can be up to 600%) in analogs of insoluble organic matter that is present in chondrites. However, the electron irradiation effects on silicate minerals are shown to be much smaller (fractionation of D/H is <200%). Particularly, fractionation of hydrogen isotopes caused by the electron irradiation in the silicate minerals larger than 10  $\mu$ m is supposed to be <20% (Roskosz et al. 2016). In our case, the measured orthopyroxenes in the OCs are all larger than 10  $\mu$ m in size. More importantly, because these measured minerals are most likely the remnants of originally crystallized larger chondrules, the fractionation of D/H in the original large chondrules would be even smaller. Therefore, we argue for negligible modification of the hydrogen isotopic compositions caused by the electron irradiation.

(ii) Galactic cosmic-ray spallation. Along with electron irradiation, spallation reactions triggered by the high-energy GCRs could occur at the planetesimal stage. The spallation reactions are responsible for the formation of secondary protons and generally limited to the surfaces of asteroid bodies (about 2–3 m; Füri et al. 2017). The amount of secondary particles produced in this mechanism is correlated with the exposure age and production rates. Using the reported exposure ages of OC meteorites (10–70 Ma; Marti & Graf 1992) and the production rates of hydrogen (4 × 10<sup>-10</sup> mol g<sup>-1</sup> Ma<sup>-1</sup>; Merlivat et al. 1976) and deuterium (2.17 × 10<sup>-12</sup> mol g<sup>-1</sup> Ma<sup>-1</sup>; Füri et al. 2017), we calculated the production rate of water. The results show small effects on both water contents and hydrogen isotopes: less than 1 ppm water could have been produced by GCR spallation, and the resulting hydrogen isotopic fractionation ranges from 1% to 26% with an average

value of  $8\%_c$ , which is within the analytical uncertainties  $(14\%_c-46\%_c, 1\sigma)$ .

(iii) Heating events. In OC parent bodies, heat can be produced by either decay of short-lived radionuclides, i.e., <sup>26</sup>Al and <sup>60</sup>Fe, which results in thermal metamorphism in planetesimals (Huss et al. 2006; see Section 4.2 for an extended discussion on thermal metamorphism), or impacts that cause localized high post-shock temperatures (Sharp & DeCarli 2006). In both these scenarios, high temperatures have been widely invoked to account for the dehydration of NAMs. Since hydrogen generally has higher diffusion rate than that of deuterium under the same physiochemical conditions, an elevation of D/H ratio is expected to exhibit along with the loss of water from NAMs. Additionally, a negative correlation between the D/H ratios and water contents of dehydrated minerals is expected after experiencing high-temperature events resulting in H loss. However, Chelyabinsk and Benenitra show no specific trend between the D/H ratios and water contents (Figure 4). Therefore, the variations of D/H ratios and water contents are not a result of dehydration during thermal metamorphism or impacts.

Rather than the dehydration of NAMs under high temperatures, NAMs could have received a fraction of water from the interstitial mesostases or matrix, as the latter components of unequilibrated chondrites can contain considerable amounts of water. Large variations in water contents of the chondrule mesostases from type 3 OCs (Bishunpur and Semarkona) have been reported (0.0008-1.51 wt.%; Figure 5; Stephant et al. 2017; Shimizu et al. 2021). The  $\delta D_{SMOW}$  values of this water range from -166% to 15,000% (Stephant et al. 2017; Shimizu et al. 2021). Besides,  $\delta D_{SMOW}$  values of the phyllosilicate in the matrix of the type 3 OC Semarkona have a large range, and the upper limit can be up to  $\sim$ 10,000% (Figure 5; Piani et al. 2015). Therefore, along with the recrystallization of silicate components in the mesostases and matrix, varying degrees of mixing of water in both NAMs and the interstitial components would have resulted in the variable D/H ratios and water contents observed in Benenitra and Chelyabinsk NAMs.

Nevertheless, several mineral grains in Benenitra and Chelyabinsk have much lower D/H ratios than the reported ones for the mesostases and matrix. This low D/H water reflects a D-poor source that has clearly been preserved in the NAMs, despite experiencing phase equilibration during thermal metamorphism. Because solar nebula is the only known reservoir characterized by a D-poor signature ( $\delta D_{SMOW} \approx$ -850%), a portion of nebular hydrogen should have been incorporated as the primordial water into NAMs. Accordingly, we define this water as nebula-sourced water. The accretion of the chondrite parent bodies likely occurred in short timescales. This requires a process that incorporates nebula-sourced water into the chondritic NAMs efficiently and quickly. Chondrules crystallized from their precursor melts in the gaseous nebula. It is possible that hydrogen gas directly dissolves into the precursor melts and subsequently is present in the chondrule crystals. However, the solubility of hydrogen in NAMs depends on the pressure subjected to the precursor melts. Petrologic experiments show that high pressures (>20 kbar) are required for NAMs to contain more than 200 ppm water (Mierdel et al. 2007). Thus, in the low-pressure nebular environment ( $10^{-3}$  bars; Galy et al. 2000), hydrogen cannot be significantly introduced into the chondritic NAMs via an igneous process. Alternatively, hydrogen implantation is

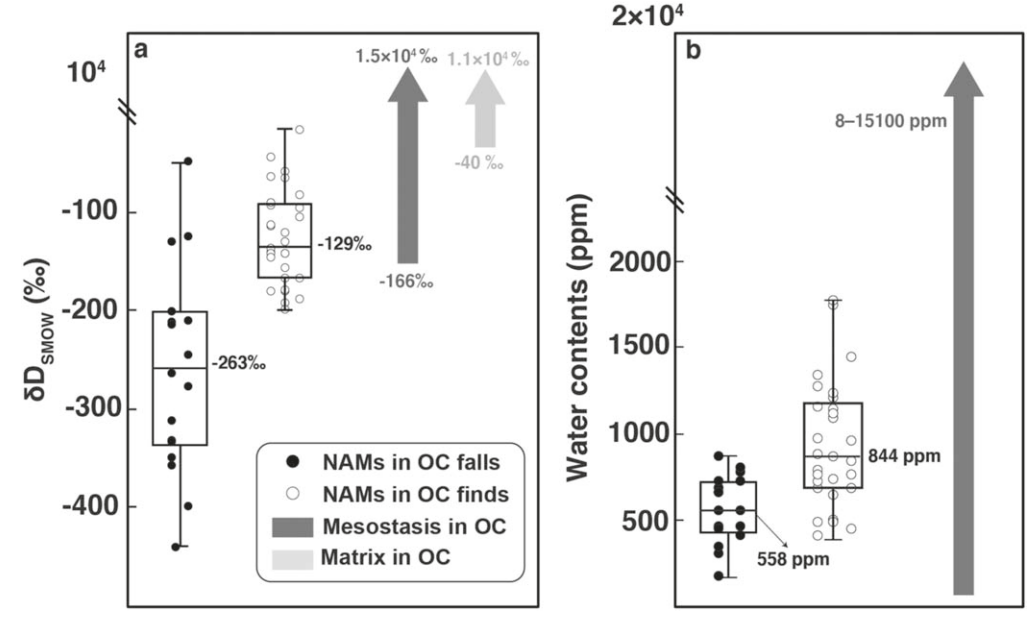


Figure 5. Box-and-whisker plots of measured (a)  $\delta D_{SMOW}$  values and (b) water contents. The interquartile range covering values between the first and third quartile of a data set is indicated by the box. The upper and lower whiskers represent data set numbers outside the interquartile range. The solid line in each box indicates the median value of a data set. The interquartile ranges of water contents and  $\delta D_{SMOW}$  values of minerals in OC finds are higher than those of minerals in OC falls. Interstitial components of chondrites, e.g., mesostasis and matrix, generally have large variations of D/H ratios and water contents. Data of the interstitial components are from Piani et al. (2015), Stephant et al. (2017), and Shimizu et al. (2021).

responsible for the incorporation of the nebula-sourced water (Jin & Bose 2021). We then modeled the D/H variation observed in the measured NAMs assuming that it was the result of the two-component mixing between the nebula-sourced D-poor water in the minerals and D-rich water in mesostases and matrix, based on the equation

$$\delta D_{MIX} = \delta D_P f + \delta D_M (1 - f), \tag{3}$$

where  $\delta D_{MIX}$  is the measured  $\delta D_{SMOW}$  value of the mineral from OC falls;  $\delta D_P$  and  $\delta D_M$  are the reported  $\delta D_{SMOW}$  values of primordial nebular hydrogen (-850%; Geiss & Gloeckler 1998) and the water in mesostases or matrix of OCs (-166%eto +10,000%; Piani et al. 2015; Stephant et al. 2017); and f denotes the proportion of primordial water in the silicate minerals of OC falls. The  $\delta D_M$  values and contents of water in the mesostases and matrix cover a large range. If we use the lowest reported  $\delta D_{SMOW}$  value of the mesostasis (-166%), up to 45% of the water in the measured silicate minerals  $(\delta D_{SMOW} = -400\%)$  is the primordial nebula-sourced component. However, if we assume that  $\delta D_M$  resembles that of the D-rich phyllosilicates ( $\delta D_{SMOW} = \sim 10,000\%$ ), during the mixing, more than 95% of the measured water is thus the primordial nebula-sourced water. Chondrule minerals may have received variable amounts of nebular-sourced water because of the stochastic nature of the implantation—diffusion process. Besides, the water contents and hydrogen isotope variations in the matrix are large. Thus, we argue that the observed variability in D/H ratios likely resulted during parentbody thermal metamorphism.

To summarize, our results, together with previously reported ones (e.g., Piani et al. 2020), argue that the water storage capability of chondritic pyroxene mineral is high. The water in OC pyroxenes is a mix of the D-poor nebula-sourced water and D-rich water from interstitial chondritic components. The low

D/H ratios of some pyroxenes in OC falls Benenitra and Chelyabinsk indicate a large fraction (45%–95%) of the nebula-sourced water ( $\delta D_{SMOW} = -850\%$ ). Electron irradiation and GCR spallation have barely modified the hydrogen component in the measured NAMs.

## 4.2. The Bulk Water Content of Benenitra and Chelyabinsk Parent Bodies

Considering the planetesimal as a whole, high temperatures have the ability to drive water/hydrogen out and reduce the bulk content of water. In a recent model proposed by Gail & Trieloff (2019), the parent body of the L/LL group of OCs is suggested to have a general radius of 115 km. From the center to the surface, the parent body is divided into type 6 (>17.5 km in depth), type 5 (9.3–17.5 km), type 4 (6.4–9.3 km), and type 3 (<6.4 km in depth) materials (Figure 6). The interiors of the planetesimals have experienced prolonged metamorphism with higher peak temperatures, albeit with slow cooling rates. To estimate the amount of water that can be lost during thermal metamorphism in asteroid bodies, we built a hydrogen-diffusion model based on the corresponding solution to Fick's second law for spherical geometry (Ingrin 2006):

$$F = 1 - \frac{6}{\pi^2} \sum_{n=1}^{\infty} \frac{1}{n^2} \exp\left(\frac{-D_{\text{eff}} n^2 \pi^2 t}{d^2}\right),\tag{4}$$

where F is the fraction of the residual water/hydrogen in the materials after thermal metamorphism; t (s) is the duration of the diffusion process caused by thermal metamorphism and adopted as 10 Ma, 25 Ma, and 75 Ma for petrologic types 4–6 materials; d (m) is the distance of the minerals to the surface of the parent body; and n denotes natural numbers.  $D_{\rm eff}$  is the effective diffusivity of the diffusing species in a porous parent

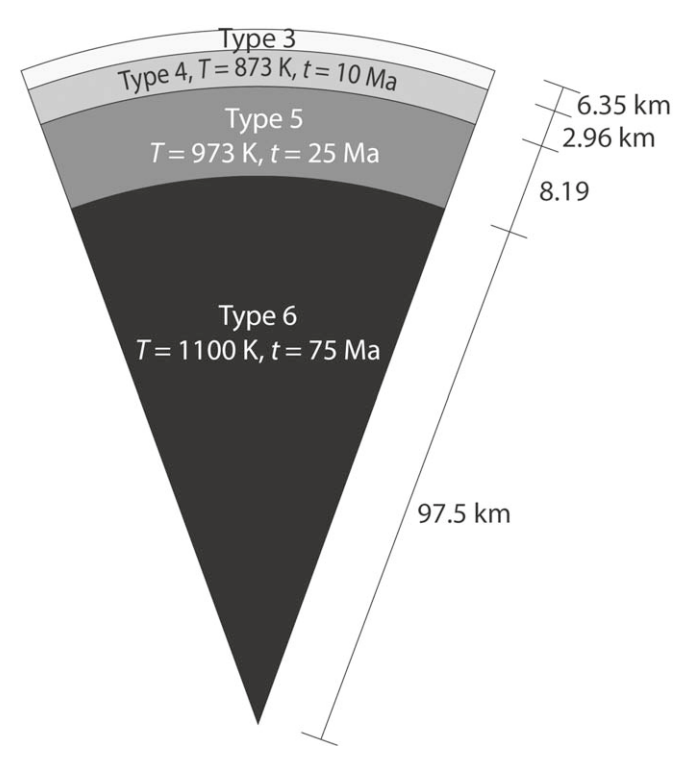


**Figure 6.** Model of the L (LL) group chondrite parent body used for the H diffusion simulations. The thickness and peak temperatures of each type of material are from Gail & Trieloff (2019). The duration (*t*) of the thermal metamorphism is adopted when the temperatures are higher than 600 K.

body and is indicated by

$$D_{\rm eff} = D_0 \exp\left(\frac{-\Delta H}{R_g T}\right) \frac{\psi}{\tau},\tag{5}$$

where  $D_0$  (m² s<sup>-1</sup>) is the diffusive coefficient for H in a specific material and  $\Delta H$  (J mol<sup>-1</sup>) is the activation enthalpy.  $R_g$  is the gas constant (8.314 J mol<sup>-1</sup> K<sup>-1</sup>), and T (K) is the temperature at which diffusion took place. The porosity ( $\psi$ ) of the parent body was assumed as 10% in our simulations, based on the analyses of 285 OCs (Consolmagnos et al. 1998). The tortuosity ( $\tau$ ) of the parent body was set as 1.5 according to the ultrasound measurements for four OCs (El Abassi et al. 2013). We searched the literature for published experimental data of  $D_0$  and  $\Delta H$  for olivine, diopside, and enstatite (Mackwell & Kohlstedt 1990; Hercule & Ingrin 1999; Demouchy & Mackwell 2003; Stalder & Skogby 2003; Sun et al. 2019; Lloyd et al. 2016) and calculated the  $D_{\rm eff}$  (6.7 × 10<sup>-16</sup> m² s<sup>-1</sup> to 1.5 × 10<sup>-10</sup> m² s<sup>-1</sup>) in a temperature range of 873–1100 K.

Our calculations show that the fraction of residual water in petrologic type 4 and 5 materials is above 98% (Figure 7). Type 6 material in the central regions of an undifferentiated body would lose <12% water, even with a thermal history of  $\sim75$  Ma (Figure 7). We also simulated the same process based on another OC parent-body model that proposes an 85 km-inradius parent body with a somewhat different thermal profile (Miyamoto et al. 1982), and we observe that <10% water is lost during thermal metamorphism. In addition to the thermal metamorphism, heat can be locally produced by impacts and cause partial melting. Benenitra shows a low weak shock stage (S3; Gibson et al. 2021), and Chelyabisk has been moderately

shocked (Stage S4; Ozawa et al. 2014), indicating that their parent bodies have experienced impact events. However, because the cooling rates of ordinary chondritic materials are high (200–600 K per 1000 yr; Ganguly et al. 2016), the high post-shock temperatures (up to 1500 K) could not last long to drive water/hydrogen out and modify the D/H ratios of minerals. Based on our model, in a timescale of 5000 yr, the water content reduced by impacts is less than 1 ppm and the change of D/H ratios of minerals is smaller than 1‰. Thus, our models clearly show that even at high temperatures (up to 900°C) parent bodies of Benenitra and Chelyabinsk (85–115 km in radius) would not lose significant amounts of water during thermal metamorphism.

Minerals from the studied Chelyabinsk and Benenitra meteorites resemble those from the S-type asteroid Itokawa, a parent body of type 4–6 ordinary chondrites (Nakamura et al. 2011); we therefore estimated the bulk water content in OC parent bodies/S-type asteroids based on the analytical results of minerals from Benenitra, Chelyabinsk (this study), and Itokawa (Jin & Bose 2019; Chan et al. 2021). The basic assumptions in our calculations are as follows: (1) The dominant components in primitive OC parent bodies are NAMs (olivine and pyroxene), metal grains, and matrix components. However, during thermal metamorphism, the matrix and mesostasis phases were transformed into feldspars. (2) The average volume fractions of the chondrule minerals (olivine and pyroxene), feldspars, and metal grains in the metamorphized parent bodies are 85 vol.%, 10 vol.%, and 5 vol.%, respectively. (3) The mineralogical fraction between olivine and pyroxene in S-type asteroids is pyroxene/(olivine +pyroxene) = 0.3–0.4. By adopting the densities  $2.7 \text{ g cm}^{-3}$  for olivine,  $3.3 \text{ g cm}^{-3}$  for pyroxene,  $2.56 \text{ g cm}^{-3}$  for feldspar, and  $7 \text{ g cm}^{-3}$  for metal, the mass fractions of olivine, pyroxene, feldspar, and metal grains in OC parent bodies are estimated as 48 wt.%, 32 wt.%, 8 wt.%, and 11 wt.%, respectively. Olivine and plagioclase mineral grains from Itokawa have been reported to contain  $235 \pm 60$  ppm and  $993 \pm 252$  ppm, respectively (Chan et al. 2021). Water contents of pyroxene minerals measured in this study and those from Itokawa are in a range of 176–988 ppm (Jin & Bose 2019; Chan et al. 2021). Using these numbers, our calculation shows that the structurally bound water in the NAMs can account for a mass fraction of 254–518 ppm in OC parent bodies or S-type asteroids.

# 4.3. Water Delivered by S-type Asteroids to Earth and Mars

The estimated bulk water content of OC parent bodies here (254–518 ppm) is well in agreement with previously estimated water content of a bulk silicate Itokawa parent body (160–510 ppm) and further confirms that inner solar system asteroids dominantly composed of NAMs can contain a significant amount of water. These hydrous small objects are the feeding material for planets, and via accretion, Earth and Mars received different amounts of water: the total water on Earth is  $\sim\!\!3900$  ppm by weight (Peslier et al. 2017), whereas the bulk water content of Mars has been estimated as 83–320 ppm (McCubbin & Barnes 2019). Here we evaluate the amount of water that could have been introduced by S-type asteroids to Earth and Mars, based on our analytical results and the existing planet accretion models.

Earth formed inside the snowline from primarily inner solar system materials but may have acquired some fraction from beyond the snowline, especially late in its evolution

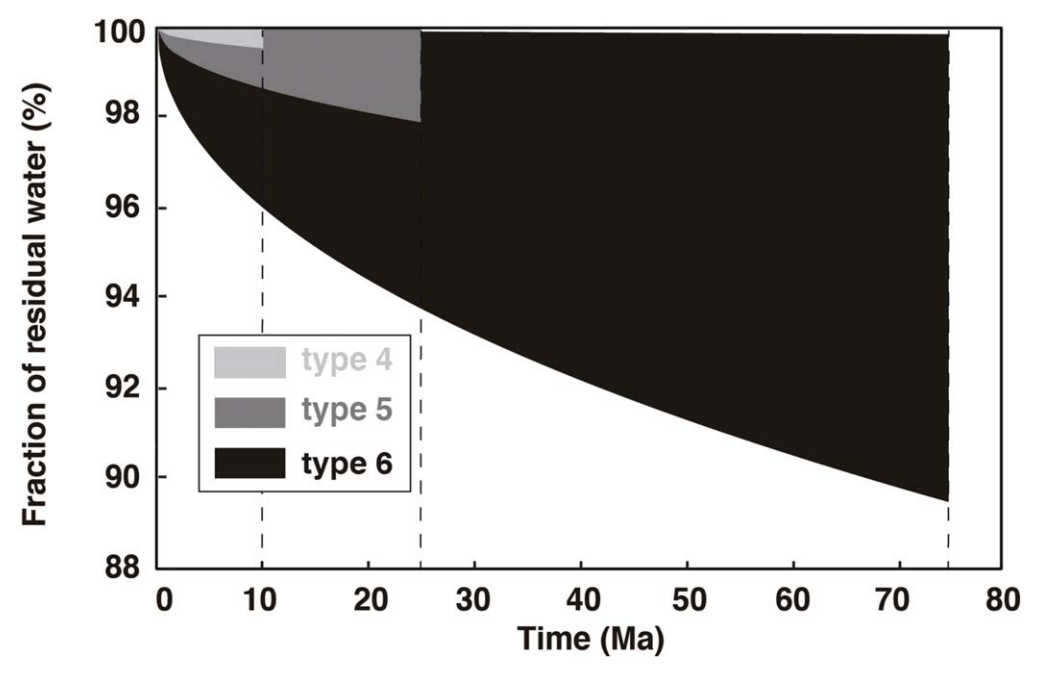


**Figure 7.** Results of the thermal-diffusion model for OCs to quantify the fraction of residual water (%) in silicate minerals after experiencing high temperatures. The model is developed based on Equations (4) and (5). The durations of the thermal metamorphism on types 4–6 are set as 10, 25, and 75 Ma; the peak temperature of the thermal metamorphism is 873 K for type 4 materials, 973 K for type 5, and 1100 K for type 6 (Gail & Trieloff 2019). The fractions of the residual water (shaded areas) in the silicate minerals after thermal metamorphism in type 4 and 5 materials are higher than 98%. Water loss from silicate minerals in type 6 materials is the largest but is still less than 12%.

(Wetherill 1990; Raymond & Izidoro 2017). In Earth's accretion model proposed by Dauphas (2017), OC materials were suggested to account for 24 wt.% of Earth's accreting materials. Using this number and the calculated bulk water content in OC parent bodies (254–518 ppm), we estimate that water delivered by the S-type asteroids during Earth's accretion accounted for a mass fraction of  $\sim$ 60–124 ppm weight, which corresponds to 0.3–0.7 times the equivalent mass of the oceans. This is comparable to the prediction by Jin & Bose (2019) that <0.5 oceans of water could have been delivered to Earth by accretion of S-type asteroids. In addition to S-type asteroids, enstatite chondrites can deliver 3 times the mass of Earth's oceans water (Piani et al. 2020).

The proportions of various chondritic materials accreted to form Mars are distinct from those for Earth. Mah & Brasser (2021) recently developed the accretion model for terrestrial planets based on the isotopic data of meteorites, as well as dynamic models of planet formation, and suggested that S-type asteroids (H chondrites) would have contributed up to 50% of the mass of proto-Mars. The water brought by these S-type asteroids likely represents the proposed D-poor reservoir that existed in the mantle of Mars (Boctor et al. 2003; Barnes et al. 2020). Assuming that parent bodies of H chondrites have an identical water content to that of the parent bodies of Chelyabinsk and Benenitra (254–518 ppm), the water delivered by S-type asteroids to Mars can account for a mass fraction of  $\sim$ 127–259 ppm, which corresponds to more than half of the current bulk water content of Mars. Then, what is the source of the remaining water in Mars?

Although Earth and Mars formed concurrently in the inner solar system, the distinct bulk water content and the amounts of water delivered by one specific accreting material likely reflect different accretion processes for these two planets. Currently, the two most widely discussed end-member accretion scenarios to form the terrestrial planets are planetesimal accretion and

pebble accretion. In the scenario of planetesimal accretion, planetary embryos grow from the accretion of kilometer- to hundreds-of-kilometer-sized planetesimals in the early stage of planet formation (e.g., Pollack et al. 1996; Hubickyj et al. 2005). In contrast, pebble accretion involves the direct accretion of millimeter- to centimeter-sized dust grains that drift past the orbits of the growing protoplanets (e.g., Johansen & Lambrechts 2017; Brouwers et al. 2019). An increasing number of studies reveal that both giant and terrestrial-sized planets could form through a combined mechanism that involves both pebble and planetesimal accretion (Alibert et al. 2018; Liu et al. 2019; Lichtenberg et al. 2021); however, the amount of the dominantly accreted solids may vary substantially from one protoplanet to another, sensitively depending on accretion chronology and the local pebble flux.

The relative contributions of pebbles and planetesimals not only influence the growth rate but also may affect the composition of the accreted material, which presents opportunities to further constrain the nature of the accreting material to the inner terrestrial planets. Inward drift of icy pebbles causes ice sublimation at the snowline, resulting in loss of water (Saito & Sirono 2011); thus, pebble-accreting embryos sample the local composition of pebbles. However, nebula-derived protoatmospheres of the planetary embryos would ablate the remaining water in the pebbles (Coleman et al. 2019). The composition inherited from planetesimals depends on both their local material composition upon gravitational collapse by the streaming instability (Drażkowska & Alibert 2017; Hyodo et al. 2021) and subsequent compositional evolution before accretion onto growing protoplanets (Ciesla et al. 2015; Lichtenberg et al. 2019). Bulk elemental abundances of the Martian core and mantle (Brennan et al. 2020) indicate that the primordial material that formed Mars was significantly more oxidized than that of Earth, which in the pebble accretion framework may be interpreted as a higher contribution of water-rich pebbles to the growing proto-Mars (Sato et al. 2016). However, the thermal requirements of core–mantle differentiation and bulk volatile fraction substantially limit the maximum amount of oxidized pebbles that can contribute to the growth of Mars (Zhang et al. 2021). In a hybrid pebbleplanetesimal accretion framework, the increased oxidation state of Mars-forming materials relative to Earth can be explained by higher contributions from early-formed, oxidized planetesimals in the inner solar system that seed the growth of the terrestrial planets (Lichtenberg et al. 2021), or secondary, minor addition of pebbles to the Mars-forming embryos when the snowline migrates inward during later disk stages (Oka et al. 2011; Sato et al. 2016). Further work aiming to constrain the nature of the planet-forming material in the inner solar system will be aided by the enhanced constraints on the bulk water fraction in meteoritic materials that we derived here.

#### 5. Conclusions

- (1) While the Antarctic OC finds show clear evidence of terrestrial contamination leading to elevated D/H ratios and water contents, the low D/H ratios detected in NAMs from fresh OC falls Chelyabinsk and Benenitra exhibit a component of primordial D-poor nebular hydrogen.
- (2) The variations of measured D/H ratio and water contents in Chelyabinsk and Benenitra are likely a result of varying degrees of water mixing between NAMs and hydrous interstitial chondritic components during parent-body processes.
- (3) Water loss in S-type asteroids during thermal metamorphism is minimal. The bulk of the water in the parent bodies of Chelyabinsk and Benenitra should survive this process, even after reaching temperatures of  $\sim 800^{\circ}$ C, and is reported to be 254–518 ppm. These water contents are consistent with the estimated water content of the Itokawa parent body.
- (4) S-type asteroids were a potential source of water on both Earth and Mars. Proto-Earth received water equivalent to 0.3–0.7 Earth's oceans primarily through accretion of S-type asteroids, while proto-Mars gained  $\sim\!127\!-\!259\,\mathrm{ppm}$  water. The existence of the nebular water component in silicate minerals (Jin & Bose 2021) and their incorporation into inner solar system objects reduce the need for a late water delivery to the terrestrial planets.
- (5) Mars may have have received most of its water from accretion of early-formed, oxidized planetesimals, with a minor addition of icy pebbles to the Mars-forming embryos, when the snowline migrated inward during later disk phases.

We thank Philipp Heck at the Field Museum for providing fresh fragments of ordinary chondrite falls, Johnson Space Center for providing thin sections of ordinary chondrite finds, and the Smithsonian Institution and Kathryn M. Kumamoto at Stanford University for the standard samples. We would like to profusely thank the anonymous reviewers for providing constructive comments and suggestions that helped improve the manuscript. Axel Wittmann and Richard L. Hervig (NSF EAR grant 1819550) are thanked for their assistance with electron probe and IMS 6f operations at ASU. Z.J. was funded by the startup funds from the State Key lab of Lunar and Planetary Science of Macao University of Science and Technology. M.B. was funded by her startup funds from ASU for the analytical work. T.L. was supported by a grant

from the Simons Foundation (SCOL award No. 611576). G.D. M. acknowledges support from ANID—Millennium Science Initiative—ICN12\_009. This material is based on work supported by the National Aeronautics and Space Administration under agreement No. 80NSSC21K0593 for the program "Alien Earths." The results reported herein benefitted from collaborations and/or information exchange within NASA's Nexus for Exoplanet System Science (NExSS) research coordination network sponsored by NASA's Science Mission Directorate.

#### **ORCID iDs**

Ziliang Jin https://orcid.org/0000-0002-1852-9362
Maitrayee Bose https://orcid.org/0000-0002-7978-6370
Tim Lichtenberg https://orcid.org/0000-0002-3286-7683
Gijs D. Mulders https://orcid.org/0000-0002-1078-9493

#### References

Alexander, C. O., Bowden, R., Fogel, M., et al. 2012, Sci, 337, 721

```
Alibert, Y., Venturini, J., Helled, R., et al. 2018, NatAs, 2, 873
Altwegg, K., Balsiger, H., Bar-Nun, A., et al. 2015, Sci, 347, 1261952
Barnes, J. J., McCubbin, F. M., Santos, A. R., et al. 2020, NatGe, 13, 260
Bell, D. R., & Ihinger, P. D. 2000, GeCoA, 64, 2109
Bell, D. R., & Rossman, G. R. 1992, Sci, 255, 1391
Boctor, N., Alexander, C., Wang, J., & Hauri, E. 2003, GeCoA, 67, 3971
Brennan, M. C., Fischer, R. A., & Irving, J. C. 2020, E&PSL, 530, 115923
Brouwers, M. G., Vazan, A., & Ormel, C. W. 2019, A&A, 621, C1
Chan, Q., Stephant, A., Franchi, I., et al. 2021, NatSR, 11, 1
Ciesla, F. J., Mulders, G. D., Pascucci, I., & Apai, D. 2015, ApJ, 804, 9
Coleman, G. A., Leleu, A., Alibert, Y., & Benz, W. 2019, A&A, 631, A7
Consolmagnos, G. J., Britt, D. T., & Stoll, C. P. 1998, M&PS, 33, 1221
Cottini, V., Ignatiev, N., Piccioni, G., et al. 2012, Icar, 217, 561
Crozaz, G., Floss, C., & Wadhwa, M. 2003, GeCoA, 67, 4727
Dauphas, N. 2017, Natur, 541, 521
Demouchy, S., & Mackwell, S. 2003, PCM, 30, 486
Drażkowska, J., & Alibert, Y. 2017, A&A, 608, A92
El Abassi, D., Ibhi, A., Faiz, B., & Aboudaoud, I. 2013, JGE, 10, 55003
Fischer-Gödde, M., & Kleine, T. 2017, Natur, 541, 525
Füri, E., Deloule, E., & Trappitsch, R. 2017, E&PSL, 474, 76
Gail, H.-P., & Trieloff, M. 2019, A&A, 628, A77
Galy, A., Young, E. D., Ash, R. D., & O'Nions, R. K. 2000, Sci, 290, 1751
Ganguly, J., Tirone, M., & Domanik, K. 2016, GeCoA, 192, 135
Geiss, J., & Gloeckler, G. 1998, in Primordial Nuclei and their Galactic
   Evolution, ed. N. Prantzos et al. (Berlin: Springer), 239
Gibson, R. L., Marais, T., Ashwal, L. D., et al. 2021, SAJSc, 117, 1
Gillmann, C., Golabek, G. J., Raymond, S. N., et al. 2020, NatGe, 13, 265
Halliday, A. N. 2013, GeCoA, 105, 146
Hartogh, P., Lis, D. C., Bockelée-Morvan, D., et al. 2011, Natur, 478, 218
Hauri, E. H., Gaetani, G. A., & Green, T. H. 2006, E&PSL, 248, 715
Hercule, S., & Ingrin, J. 1999, AmMin, 84, 1577
Hirschmann, M., Withers, A., Ardia, P., & Foley, N. 2012, E&PSL, 345, 38
Hirschmann, M. M. 2016, AmMin, 101, 540
Hubickyj, O., Bodenheimer, P., & Lissauer, J. J. 2005, Icar, 179, 415
Huss, G. R., Rubin, A. E., & Grossman, J. N. 2006, in Meteorites and the Early
   Solar System II, ed. D. S. Lauretta & H. Y. McSween, Jr. (Tucson, AZ:
   Univ. Arizona Press), 567
Hutsemekers, D., Manfroid, J., Jehin, E., Zucconi, J.-M., & Arpigny, C. 2008,
     &A. 490, L31
Hyodo, R., Guillot, T., Ida, S., Okuzumi, S., & Youdin, A. N. 2021, A&A,
   646, A14
Ikoma, M., & Genda, H. 2006, ApJ, 648, 696
Ingrin, J. 2006, RvMG, 62, 291
Jin, Z., & Bose, M. 2019, SciA, 5, eaav8106
Jin, Z., & Bose, M. 2021, ApJ, 913, 116
Johansen, A., & Lambrechts, M. 2017, AREPS, 45, 359
Kaeter, D., Ziemann, M. A., Böttger, U., et al. 2018, M&PS, 53, 416
Kumamoto, K. M., Warren, J. M., & Hauri, E. H. 2017, AmMin, 102, 537
Lammer, H., Zerkle, A. L., Gebauer, S., et al. 2018, A&ARv, 26, 2
Laurent, B., Roskosz, M., Remusat, L., et al. 2015, NatCo, 6, 8567
Lawrence, D. J., Feldman, W. C., Goldsten, J. O., et al. 2013, Sci, 339, 292
```

```
Lichtenberg, T., Drażkowska, J., Schönbächler, M., Golabek, G. J., &
  Hands, T. O. 2021, Sci, 371, 365
Lichtenberg, T., Golabek, G. J., Burn, R., et al. 2019, NatAs, 3, 307
Liu, B., Ormel, C. W., & Johansen, A. 2019, A&A, 624, A114
Lloyd, A. S., Ferriss, E., Ruprecht, P., et al. 2016, JPet, 57, 1865
Mackwell, S. J., & Kohlstedt, D. L. 1990, JGR, 95, 5079
Mah, J., & Brasser, R. 2021, Icar, 354, 114052
Mane, P., Hervig, R., Wadhwa, M., et al. 2016, M&PS, 51, 2073
Marti, K., & Graf, T. 1992, AREPS, 20, 221
McCubbin, F. M., & Barnes, J. J. 2019, E&PSL, 526, 115771
Meisel, T., Walker, R., & Morgan, J. 1996, Natur, 383, 517
Merlivat, L., Lelu, M., Nief, G., & Roth, E. 1976, LPSC, 7, 649
Mierdel, K., Keppler, H., Smyth, J. R., & Langenhorst, F. 2007, Sci, 315,
Miyamoto, M., Fujii, N., & Takeda, H. 1982, LPSC, 12, 1145
Nakamura, T., Noguchi, T., Tanaka, M., et al. 2011, Sci, 333, 1113
Oka, A., Nakamoto, T., & Ida, S. 2011, ApJ, 738, 141
Orosei, R., Lauro, S., Pettinelli, E., et al. 2018, Sci, 361, 490
Owen, J. E. 2019, AREPS, 47, 67
Ozawa, S., Miyahara, M., Ohtani, E., et al. 2014, NatSR, 4, 5033
Peslier, A. H., Schönbächler, M., Busemann, H., & Karato, S.-I. 2017, SSRv,
Piani, L., Marrocchi, Y., Rigaudier, T., et al. 2020, Sci, 369, 1110
Piani, L., Robert, F., & Remusat, L. 2015, E&PSL, 415, 154
```

```
Pollack, J. B., Hubickyj, O., Bodenheimer, P., et al. 1996, Icar, 124, 62
Raymond, S. N., & Izidoro, A. 2017, Icar, 297, 134
Roskosz, M., Laurent, B., Leroux, H., & Remusat, L. 2016, ApJ, 832, 55
Rossman, G. R., Bell, D. R., & Ihinger, P. D. 1995, AmMin, 80, 465
Saal, A. E., Hauri, E. H., Van Orman, J. A., & Rutherford, M. J. 2013, Sci,
Saito, E., & Sirono, S.-i. 2011, ApJ, 728, 20
Sarafian, A. R., Nielsen, S. G., Marschall, H. R., McCubbin, F. M., &
  Monteleone, B. D. 2014, Sci, 346, 623
Sato, T., Okuzumi, S., & Ida, S. 2016, A&A, 589, A15
Sharp, T. G., & DeCarli, P. S. 2006, in Meteorites and the Early Solar System
  II, ed. D. S. Lauretta & H. Y. McSween, Jr. (Tucson, AZ: Univ. Arizona
  Press), 653
Sharp, Z. D. 2017, ChGeo, 448, 137
Shimizu, K., Alexander, C. M., Hauri, E. H., et al. 2021, GeCoA, 301, 230
Stalder, R., & Skogby, H. 2003, PCM, 30, 12
Stephant, A., Garvie, L. A. J., Mane, P., Hervig, R., & Wadhwa, M. 2018,
    latSR, 8, 12385
Stephant, A., Remusat, L., & Robert, F. 2017, GeCoA, 199, 75
Sun, W., Yoshino, T., Kuroda, M., Sakamoto, N., & Yurimoto, H. 2019,
  JGRB, 124, 5696
Velbel, M. A. 2014, M&PS, 49, 154
Wetherill, G. W. 1990, AREPS, 18, 205
Zhang, Z., Bercovici, D., & Jordan, J. S. 2021, JGRE, 126, e06754
```